RSC Advances

PAPER



Cite this: *RSC Adv.*, 2023, **13**, 21754

# Synthesis of AgBr/$Ti_3C_2$@$TiO_2$ ternary composite for photocatalytic dehydrogenation of 1,4-dihydropyridine and photocatalytic degradation of tetracycline hydrochloride

Hanliu Wu,[a] Yan Quan,[a] Meiling Liu,[a] Xuemei Tian,[a] Chunguang Ren[b] and Zhonghua Wang *[a]

In this work, AgBr/$Ti_3C_2$@$TiO_2$ ternary composite photocatalyst was prepared by a solvothermal and precipitation method with the aims of introducing $Ti_3C_2$ as a cocatalyst and $TiO_2$ as a compositing semiconductor. The crystal structure, morphology, elemental state, functional groups and photoelectrochemical properties were studied by XRD, SEM, TEM, XPS, FI-IR and EIS. The photocatalytic performances of the composites were investigated by the photodehydrogenation of diethyl 1,4-dihydro-2,6-dimethyl-3,5-pyridinedicarboxylate (1,4-DHP) and the photodegradation of tetracycline hydrochloride (TCH) under visible light irradiation ($\lambda$ > 400 nm). The AgBr/$Ti_3C_2$@$TiO_2$ composite photocatalyst showed enhanced photocatalytic performance in both photocatalytic reactions. The photocatalytic activity of the composite photocatalyst is dependent on the proportional content of $Ti_3C_2$@$TiO_2$. With optimized $Ti_3C_2$@$TiO_2$ proportion, the photocatalytic ability of the AgBr/$Ti_3C_2$@$TiO_2$ composite was 24.5 times as high as that of $Ti_3C_2$@$TiO_2$ for photodehydrogenation of 1,4-DHP and 1.9 times as high as that of pure AgBr for photodegradation of TCH. The enhanced photocatalytic performance of the AgBr/$Ti_3C_2$@$TiO_2$ composite should be due to the formation of a p–n heterojunction structure between AgBr and $Ti_3C_2$@$TiO_2$ and the excellent electronic properties of $Ti_3C_2$, which enhanced the visible light absorption capacity, lowered the internal resistance, speeded up the charge transfer and reduced the recombination efficiency of photo-generated carriers. Mechanism studies showed that superoxide free radical ($^{\bullet}O_2^-$) was the main active species. In addition, the composite photocatalyst also displayed good stability, indicating its reutilization in practical application.

Received 2nd April 2023
Accepted 10th July 2023

DOI: 10.1039/d3ra02164e

rsc.li/rsc-advances

## 1. Introduction

With the rapid development of industrialization and urbanization, environmental pollution and the energy crisis have received extensive attention in the past decades.[1–3] In order to solve these problems, inexhaustible solar-driven photocatalysis is considered to be a potential green method to produce photoinduced carriers with redox ability by using semiconductors as photocatalysts.[4,5] So far, many photocatalysts have been reported in this field, such as $TiO_2$,[6,7] ZnO,[8] CdS[9,10] and g-$C_3N_4$.[11,12] Among these photocatalysts, $TiO_2$ has gained a lot of attention due to its high photocatalytic ability and good chemical stability. What's more, it is also low in price and easy to obtain, safe and harmless.[13] However, the practical application of $TiO_2$ as a photocatalyst is limited because it can only be excited by UV light that accounts for only a small fraction of the natural sunlight (~5%).[14,15] The method to overcome this shortcoming is to modify $TiO_2$ with narrow band gap semiconductors. Under light irradiation, the photogenerated charge carriers can move from one semiconductor to another, thereby enhancing the photocatalytic activity.[16–18]

AgBr is an important photosensitive semiconductor for traditional use. It is an n-type semiconductor with a narrow band gap of ~2.64 eV and is very active under visible light excitation.[17] Unfortunately, the pure AgBr is quite unstable, and the photoinduced electrons will combine with $Ag^+$ to form $Ag^0$ clusters, resulting in the undesirable and uncontrolled photolysis of AgBr, which leads to the low reusability of AgBr in photocatalytic reaction.[19–21] Therefore, the composite of AgBr and $TiO_2$ can enhance the photocatalytic performance and improve the photocatalytic stability by reducing the band gap and prolonging the life of photoinduced electron–hole pairs. Abou Asi *et al.* prepared AgBr/$TiO_2$ nanocomposite by a deposition–precipitation method with the addition of cetyltrimethylammonium bromide, and evaluated the photocatalytic

[a]*Chemical Synthesis and Pollution Control Key Laboratory of Sichuan Province, College of Chemistry and Chemical Engineering, China West Normal University, Nanchong 637002, Sichuan, China. E-mail: zhwangs@163.com; Fax: +86 817-2568081; Tel: +86 817-2445233*

[b]*College of Life Sciences, Yantai University, Yantai 264005, China*

activity by the reduction of $CO_2$.[22] Cui *et al.* successfully prepared AgBr nanoparticles modified $TiO_2$ nanotube arrays (AgBr/$TiO_2$ NTAs) photoelectrode by anodic oxidation and ultrasonic assisted precipitation. The enhance photocatalytic activity of the AgBr/$TiO_2$ NTAs materials was evaluated by the degradation of 4-chlorophenol (4-CP) under visible light irradiation, and 92.6% of 4-CP degradation was obtained within 140 min of Xenon illumination.[23]

MXene, a new family of 2D transition metal carbides and/or nitrides, has attracted widespread interest since its first appearance in 2011.[24] Up to now, MXenes has been widely studied and applied in energy storage and conversion,[25] catalysis,[26] sensor,[27] heavy metal ion[28] and dye adsorption[29] and other fields. Because of the excellent conductivity and well visible light absorption capacity of $Ti_3C_2$ MXene, it has been clearly proved to be an efficient cocatalyst for improving photocatalytic activity, which can effectively promote the separation and transfer of photogenerated electrons. For example, Low *et al.* used the calcination method to grow $TiO_2$ nanoparticles *in situ* on $Ti_3C_2$ MXene with good electrical conductivity. The photocatalytic reduction of $CO_2$ to $CH_4$ (0.22 μmol $h^{-1}$) by the optimized $TiO_2/Ti_3C_2$ composite is 3.7 times higher than that of commercial $TiO_2$ (P25).[30] Moreover, Li *et al.* modified carbon nitride (CN) with $Ti_3C_2$ and found that compared with the original CN, the modified CN showed significantly improved photocatalytic activity for U(VI) reduction.[2]

To the best of our knowledge, there is no report about the enhancement of the photocatalytic performance of AgBr by compositing with $TiO_2$ and simultaneously introducing $Ti_3C_2$ as a cocatalyst. In this study, $Ti_3C_2$@$TiO_2$ was prepared by *in situ* growth of $TiO_2$ on $Ti_3C_2$ under solvothermal treatment, and a series of AgBr/$Ti_3C_2$@$TiO_2$ composites were prepared by precipitation method. The *in situ* preparation of $Ti_3C_2$@$TiO_2$ makes $Ti_3C_2$ and $TiO_2$ closely contact, and improves the separation efficiency of photogenerated electron hole pairs. The photocatalytic performance of the AgBr/$Ti_3C_2$@$TiO_2$ photocatalyst was evaluated by the photodehydrogenation of 1,4-DHP and photodegradation of TCH under visible light irradiation. The AgBr/$Ti_3C_2$@$TiO_2$ photocatalyst showed enhanced photocatalytic performance in both photocatalytic reactions. The photocatalytic performance of the AgBr/$Ti_3C_2$@$TiO_2$ composite with optimized composition is 3.9 and 24.5 times higher than that of pure AgBr and $Ti_3C_2$@$TiO_2$, respectively, for photodehydrogenation of 1,4-DHP and 1.9 and 5.9 times higher than that of pure AgBr and $Ti_3C_2$@$TiO_2$ for photodegradation of TCH. The composite photocatalyst were stable under light irradiation. The relative dehydrogenation efficiency of 1,4-DHP photolysis and the relative degradation efficiency of TCH degradation remained above 86% after four cycles.

# 2. Experimental

## 2.1. Preparation of AgBr powder

First, 1.0 g $AgNO_3$ was dissolved in 50 mL of deionized water to obtain $AgNO_3$ solution (solution A), 0.70 g KBr was mixed with 25 mL deionized water and dissolved to prepare KBr solution (solution B). Then, the solution B was added dropwise the solution A under magnetically stirring, and the mixed solution was stirred in the dark for 0.5 h. After centrifugation and washing, the AgBr precipitate was collected and dried at 60 °C.

## 2.2. Preparation of layered $Ti_3C_2$

Typically, 0.5 g $Ti_3AlC_2$ powder was added to 10 mL 30 wt% HF (within 5 min) and the reaction was allowed to proceed at room temperature for 5 h to remove the element of Al. The resulting powder was collected by centrifugation (3500 rpm, 5 min per cycle) and washed 5 times with deionized water. Then, the black precipitate was dried at 80 °C for 24 h to obtain multilayered $Ti_3C_2$.

## 2.3. Preparation of $Ti_3C_2$@$TiO_2$ by *in situ* solvothermal method

First, 0.3 g $Ti_3C_2$, which was obtained from HF etching of $Ti_3AlC_2$, was mixed with 30 mL isopropanol (IPA). After sonication for 10 min, the mixture was poured into a 100 mL Teflon-lined reactor and heated at 150 °C for 24 h. The precipitate was centrifuged, repeatedly washed until the pH value of the eluate was about 6, and then dried at 60 °C to obtain $Ti_3C_2$@$TiO_2$ sample.

## 2.4. Preparation of AgBr/$Ti_3C_2$@$TiO_2$ composites

Solution A was prepared by dissolving 0.1808 g $AgNO_3$ and dispersing 0.0225 g $Ti_3C_2$@$TiO_2$ to 50 mL deionized water. Solution B was prepared by dissolving 0.1267 g KBr to 25 mL of deionized water. Then, solution B was added dropwise to solution A under magnetic stirring. After further stirred for 2 h, the reaction mixture was centrifuged, filtered and dried at 60 °C to obtain AgBr/$Ti_3C_2$@$TiO_2$ composite. This sample was denoted as AgBr/$Ti_3C_2$@$TiO_2$-10%, for the mass percentage of $Ti_3C_2$@$TiO_2$ was accounting for 10% of the sample. Other AgBr/$Ti_3C_2$@$TiO_2$ composite samples with different proportions of $Ti_3C_2$@$TiO_2$ (10%, 20%, 30%, 40%, 50%, 60%, 70%) were prepared by changing the amount of each sample. The obtained AgBr/$Ti_3C_2$@$TiO_2$ samples were denoted as AgBr/$Ti_3C_2$@$TiO_2$-*x*% (*x*% referred to the mass percentage of $Ti_3C_2$@$TiO_2$).

## 2.5. Characterization

The crystal structure, morphology, and elemental composition were characterized by X-ray diffraction (XRD), scanning electron microscopy (SEM), high-resolution transmission electron microscopy (HRTEM), energy dispersive spectrometer (EDS), X-ray photoelectron spectroscopy (XPS) and Fourier transform infrared spectrometer (FT-IR). An electrochemical workstation equipped with a three-electrode system was used to measure the electrochemical characteristics of the samples.

## 2.6. Photocatalytic performance evaluation

The photocatalytic performance of AgBr/$Ti_3C_2$@$TiO_2$ was evaluated by the photodehydrogenation of 1,4-DHP and photodegradation of TCH under the irradiation of visible light. The light was provided by a 70 W metal halide lamp equipped with a 400 nm cutoff filter. Typically, 50 mg of AgBr/$Ti_3C_2$@$TiO_2$

composite was dispersed into 50 mL of 0.1 mM 1,4-DHP or 20 mg $L^{-1}$ TCH solution. In order to obtain adsorption–desorption equilibrium, the mixture was magnetically stirred for 30 min before illumination. The extent of the reaction was spectroscopically monitored by measuring the residual concentrations of 1,4-DHP and TCH at wavelengths of 374 and 357 nm, respectively.

## 3. Results and discussion

The XRD patterns of $Ti_3AlC_2$, $Ti_3C_2$, $Ti_3C_2$@$TiO_2$, AgBr and AgBr/$Ti_3C_2$@$TiO_2$ composites are shown in Fig. 1. $Ti_3C_2$ was obtained by etching $Ti_3AlC_2$ with HF, removing Al layer and retaining Ti and C layers, the XRD diffraction pattern of the precursor $Ti_3AlC_2$ shows that there was a main diffraction peak at $2\theta$ = 39.3°. After reacting with HF, the diffraction pattern had undergone the following significant changes: firstly, the peak observed at the diffraction angle of $2\theta$ = 39.3° almost disappeared, indicating that the Al layer was successfully removed by etching.[31] Secondly, at the low diffraction angle, because of the expansion of the interlayer distance, the peaks at (002) and (004) move to a low angle and become wider and weaker, indicating that $Ti_3AlC_2$ has been transformed into $Ti_3C_2$.[32,33] The characteristic peaks of multilayer $Ti_3C_2$ appear at 2θ values of 8.94° (002), 18.29° (006), 27.66° (008), 34.53° (101), 41.78° (105) and 60.62° (110), which are consistent with the literature.[34,35] $Ti_3C_2$@$TiO_2$ composites were obtained by *in situ* growth of $TiO_2$ on $Ti_3C_2$ after solvothermal treatment of $Ti_3C_2$ and isopropanol (IPA) in a reactor. The characteristic peaks at 25.28°, 36.95°, 48.04° and 55.06° were attributed to the (101), (103), (200) and (211) crystal planes of anatase $TiO_2$ (JCPDS no. 21-1272).[36] And the characteristic peaks with $2\theta$ values of 8.94°, 18.29°, 27.66°, 34.53° and 60.62° in $Ti_3C_2$@$TiO_2$ correspond to the (002), (004), (006), (101) and (110) crystal planes of $Ti_3C_2$, respectively. These results indicate that $Ti_3C_2$@$TiO_2$ composites were successfully synthesized (Fig. 1A). It can be noted from Fig. 1B that the diffraction peaks of AgBr can be attributed to the face-centered cubic crystal phase of AgBr, and the $2\theta$ values are 26.72° (111), 30.96° (200), 44.34° (220), 52.48° (311), 55.04° (222), 64.47° (400), 71.09° (331), 73.26° (420) and 81.61° (422), respectively.[17] It is consistent with the standard data of AgBr (JCPDS no. 06-0438). As for the AgBr/$Ti_3C_2$@$TiO_2$ composites, except for the XRD patterns of AgBr, another two peaks appeared at $2\theta$ values of 39.12° and 77.39°, which should be ascribed to the (111) and (311) crystal planes of $Ag^0$ (JCPDS no. 65-2871)[33,37] (Fig. 1B). With the increase of $Ti_3C_2$@$TiO_2$ content, the diffraction peaks of AgBr in the ternary composites gradually weakened, and the diffraction peaks of (111) and (311) crystal planes of Ag increased. Due to the existence of low-valent Ti with strong reducing activity in $Ti_3C_2$ solution, $Ag^+$ can be partially reduced to $Ag^0$.[33,38] It is worth noting that the XRD peaks of $Ti_3C_2$ and $TiO_2$ were not observed in the XRD patterns of AgBr/$Ti_3C_2$@$TiO_2$ composites, which may have resulted from their low degree of crystallization in the composite samples.[39,40]

As shown in Fig. 2A and B, due to the exothermic reaction of HF, $Ti_3AlC_2$ transforms from a dense, layered ternary carbide structure to an accordion-like structure of $Ti_3C_2$.[35] After co-heat treatment of $Ti_3C_2$ and isopropanol (IPA) in a reactor, $TiO_2$ nanosheets with a size of about 100 nm were *in situ* grown on the surface of multilayer $Ti_3C_2$ to form $Ti_3C_2$@$TiO_2$ composites (Fig. 2C). The AgBr sample shows that irregular polyhedrons with a size of about 2–4 μm were clustered together (Fig. 2D). Compared with pure AgBr (Fig. 2D), AgBr particles in AgBr/$Ti_3C_2$@$TiO_2$-10% samples showed better dispersibility and smaller size (Fig. 2E). With the increase of $Ti_3C_2$@$TiO_2$ content, the shape of irregular polyhedral AgBr particles becomes more dispersed and the particle size becomes smaller (Fig. 2F). These results indicate that the addition of $Ti_3C_2$@$TiO_2$ not only affects the morphology and size of AgBr particles, but also prevents the agglomeration of AgBr polyhedral.

The microstructure of AgBr/$Ti_3C_2$@$TiO_2$-40% composite was further analyzed by TEM and HRTEM. As shown in Fig. 3A and B, AgBr is in close contact with the $Ti_3C_2$@$TiO_2$ sheets. According to Fig. 3C, the lattice fringe spacing of 0.189 nm and 0.204 nm correspond to the $TiO_2$ (200) and AgBr (200) crystal planes, respectively. The lattice fringe spacings of 0.189 nm and 0.230 nm belong to $TiO_2$ (200) and $Ti_3C_2$ (103) crystal planes, respectively[31] (Fig. 3E). Furthermore, the lattice fringes at

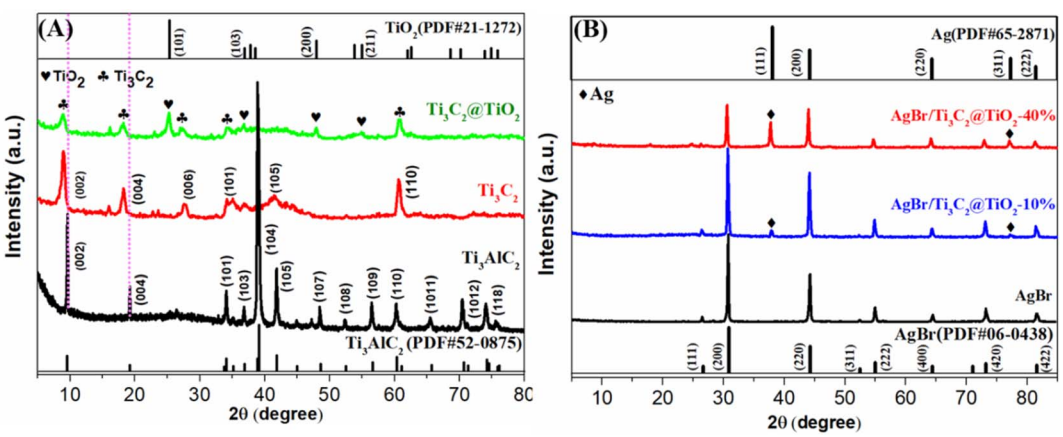


Fig. 1 XRD patterns of $Ti_3AlC_2$, $Ti_3C_2$ and $Ti_3C_2$@$TiO_2$ (A), AgBr and AgBr/$Ti_3C_2$@$TiO_2$ composites (B).

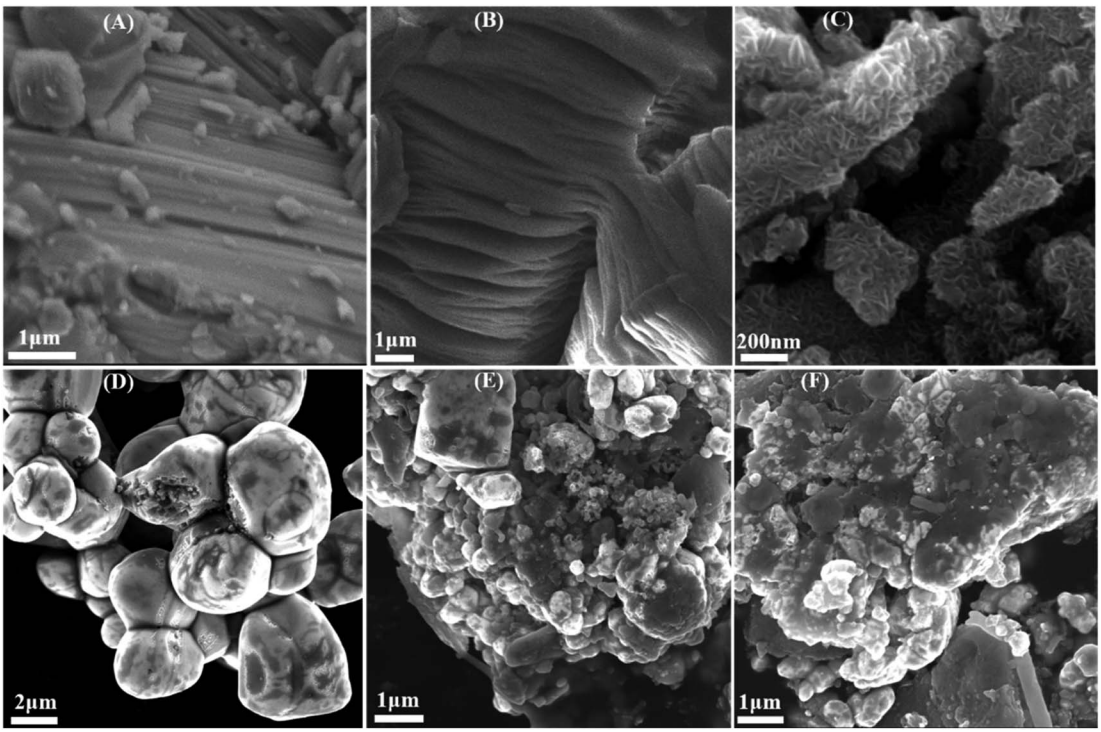


Fig. 2 SEM images of $Ti_3AlC_2$ (A), $Ti_3C_2$ (B), $Ti_3C_2$@$TiO_2$ (C), AgBr (D), AgBr/$Ti_3C_2$@$TiO_2$-10% (E), AgBr/$Ti_3C_2$@$TiO_2$-40% (F).

0.214 nm and 0.204 nm correspond to $Ti_3C_2$ (005) and Ag (200) crystal planes, respectively[41] (Fig. 3D and F). The above data show that after solvothermal method and precipitation method, stable heterojunctions are formed between AgBr and $TiO_2$, thus improving the photocatalytic performance of the composites.[42]

The element distribution and composition of the composites were detected by elemental mapping image. Fig. 4 shows the elemental scanning spectrum of AgBr/$Ti_3C_2$@$TiO_2$-10% composites. As can be seen from the figure, the distribution of six elements, namely C, Ag, Br, O, Ti and F. Among them, the element F is the residue of $Ti_3AlC_2$ etched by HF, so its content is less.

The full XPS spectra (Fig. 5A) shows the characteristic peaks of Ti, C, O, Ag and Br in AgBr/$Ti_3C_2$@$TiO_2$-40% sample. Fig. 5B–

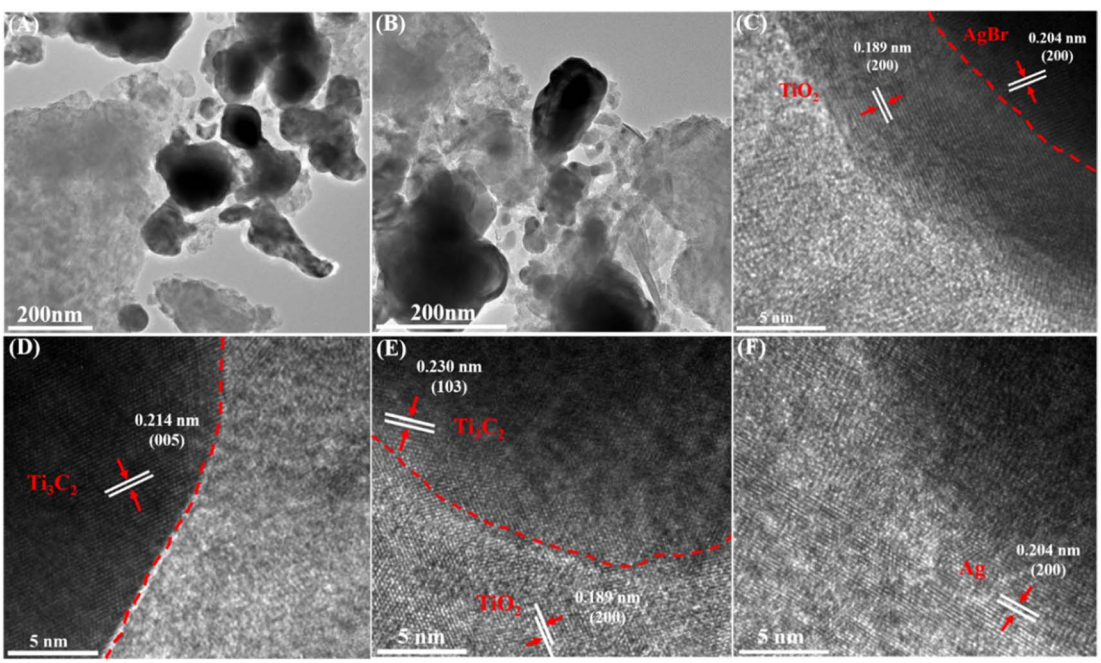


Fig. 3 TEM (A and B) and HRTEM (C, D, E and F) images of AgBr/$Ti_3C_2$@$TiO_2$-40% sample.

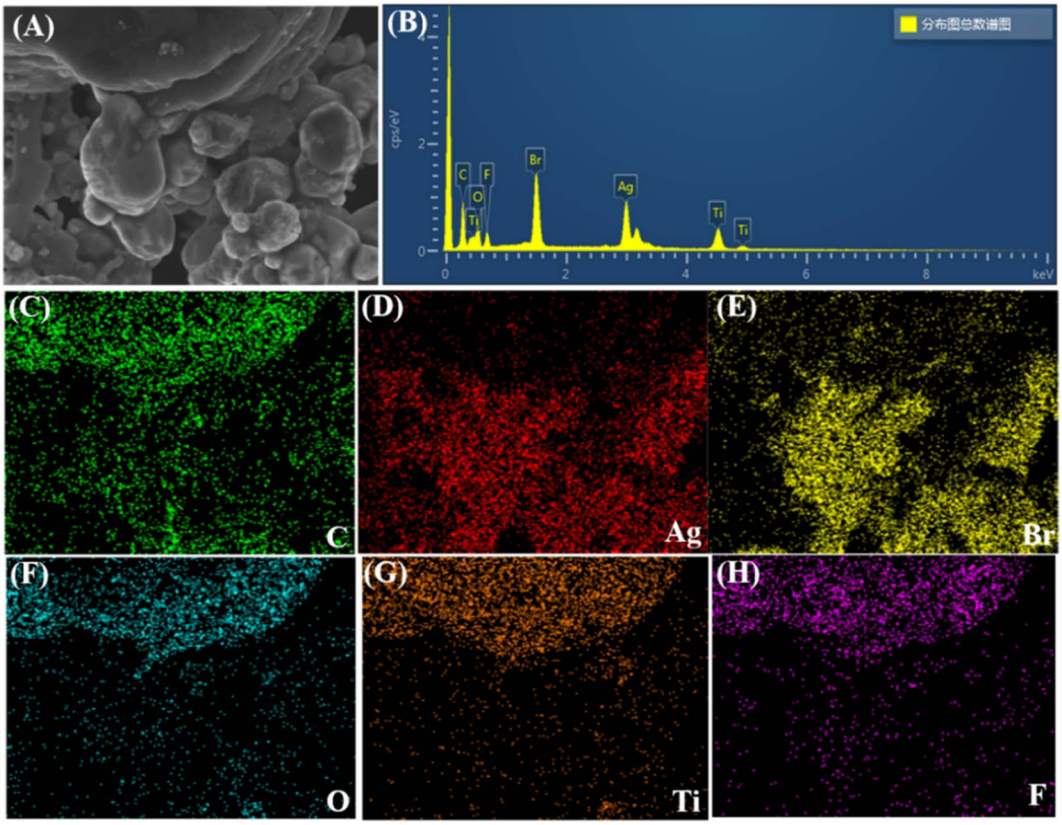


Fig. 4 Selected SEM images (A), the EDS spectrum of the AgBr/$Ti_3C_2$@$TiO_2$-10% composite (B), C (C), Ag (D), Br (E), O (F), Ti (G) and F (H) element.

F shows the high-resolution spectra of each element. After carbon correction, curve fitting and background subtraction are carried out. As shown in Fig. 5B, five different peaks can be found in high resolution Ti 2p, of which 455.1 eV, 456.5 eV and 459.0 eV belong to Ti $2p_{3/2}$, 464.8 eV and 461.6 eV attribute to Ti $2p_{1/2}$. Specifically, the peaks at 456.5 eV, 459.0 eV and 464.8 eV can be belonged to Ti–O bond, and the peaks at 455.1 eV and 461.6 eV indicate the existence of Ti–C bond.[43,44] The XPS C 1s spectrum of the composite (Fig. 5C) showed a strong peak at the binding energy of 284.8 eV, corresponding to the C–C bond.

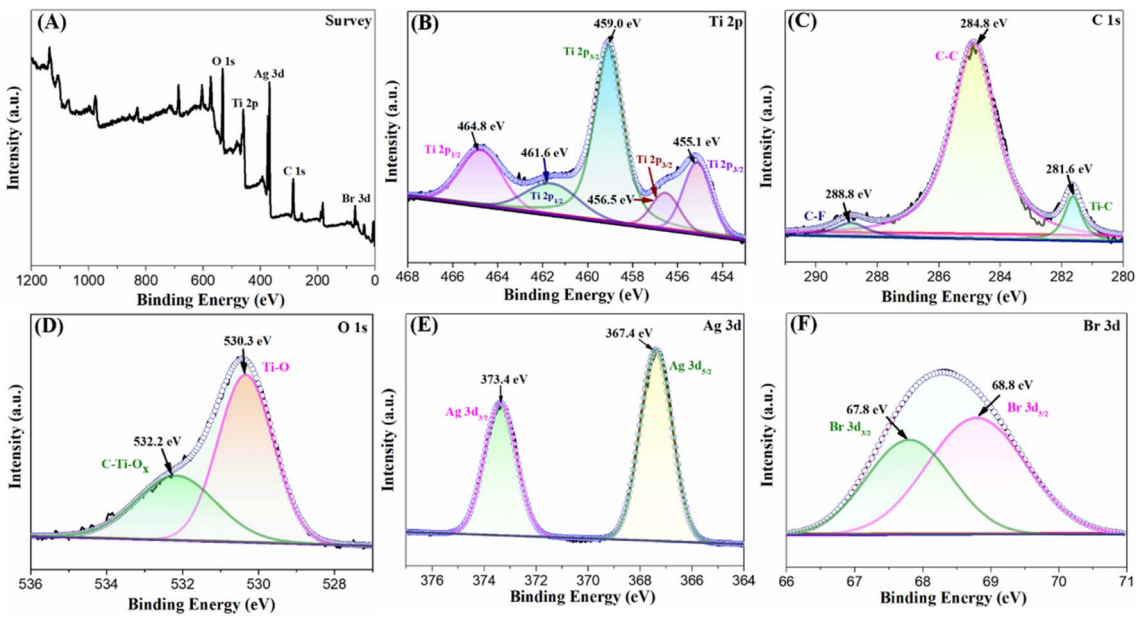


Fig. 5 High-resolution XPS spectra of the AgBr/$Ti_3C_2$@$TiO_2$-40%. Full spectrum (A), Ti 2p (B), C 1s (C), O 1s (D), Ag 3d (E) and (F) Br 3d.

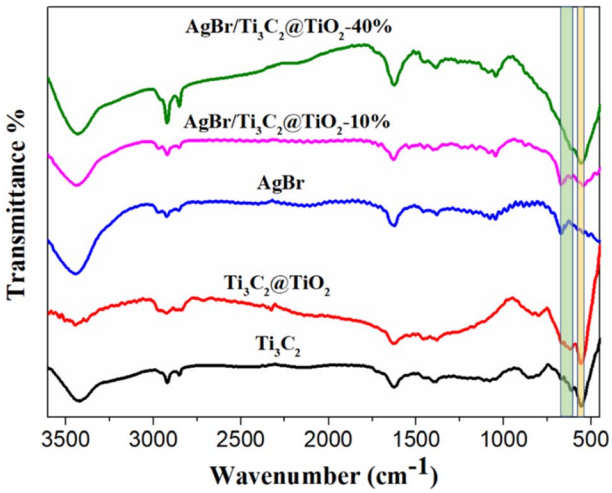


Fig. 6 FT-IR spectra of $Ti_3C_2$, $Ti_3C_2$@$TiO_2$, AgBr, AgBr/$Ti_3C_2$@$TiO_2$-10% and AgBr/$Ti_3C_2$@$TiO_2$-40% samples.

Two peaks appear at the binding energies of 281.6 eV and 288.8 eV, corresponding to the Ti–C bond and the C–F bond, respectively.[43,45] In addition, the O 1s XPs spectrum showed two distinct peaks at 532.2 eV and 530.3 eV (Fig. 5D), the highest peak at 530.3 eV usually represent the lattice oxygen in $TiO_2$, which also indicated that $TiO_2$ was successfully grown *in situ* on $Ti_3C_2$.[31] Fig. 5E shows the Ag 3d spectrum. There are two peaks at around 367.4 eV and 373.4 eV, which can be attributed to Ag $3d_{5/2}$ and Ag $3d_{3/2}$, respectively. Other studies have shown that the Ag $3d_{5/2}$ and Ag $3d_{3/2}$ peaks of $Ag^+$ in AgBr usually locate at about 367.37 and 373.48 eV, and the Ag $3d_{5/2}$ and Ag $3d_{3/2}$ peaks of $Ag^0$ are usually observed at 367.87 and 376.03 eV.[14] The present Ag 3d data (367.4 eV for Ag $3d_{5/2}$ and 373.4 eV for Ag $3d_{3/2}$) should be the superposition of the 3d binding energy of $Ag^0$ and $Ag^+$.[46] However, the peaks in Fig. 5E are difficult to divide into two sets of peaks belonging to $Ag^0$ and $Ag^+$, respectively. It may show that $Ag^0$ particles and AgBr particles have a special composite structure, which is different from any of their individual particles.[37,46] Fig. 5F shows the Br 3d XPS spectrum, the binding energies of 67.8 eV and 68.8 eV correspond to Br $3d_{3/2}$ and Br $3d_{5/2}$, respectively.[47,48]

The functional groups of $Ti_3C_2$, $Ti_3C_2$@$TiO_2$, AgBr, AgBr/$Ti_3C_2$@$TiO_2$-10% and AgBr/$Ti_3C_2$@$TiO_2$-40% were detected by FT-IR (Fig. 6). The absorption peaks appeared at 3424 $cm^{-1}$ and 1631 $cm^{-1}$, respectively, corresponding to –OH asymmetric stretching and –OH bending vibration of adsorbed water.[49] Furthermore, the band at about 2850 $cm^{-1}$–2924 $cm^{-1}$ corresponds to O–H stretching vibration, which reflects the existence of –OH.[50] In $Ti_3C_2$@$TiO_2$, the peaks at 616 $cm^{-1}$ and 564 $cm^{-1}$ correspond to Ti–O and Ti–C vibrations respectively,[26,51] and the peak at 1393 $cm^{-1}$ corresponds to C–O or C–N.[52] With the increase of $Ti_3C_2$@$TiO_2$ content, the two characteristic peaks of $Ti_3C_2$ (at 564 $cm^{-1}$–670 $cm^{-1}$) gradually increased when it was compounded with AgBr.

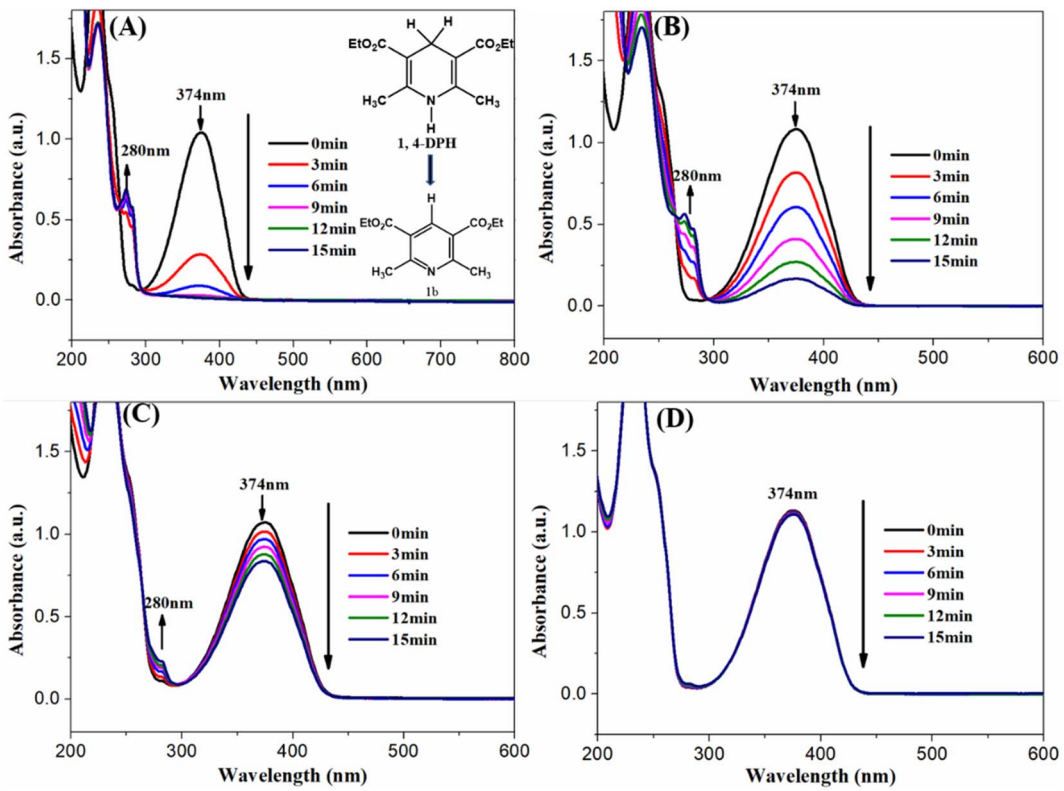


Fig. 7 Under the irradiation of visible light ($\lambda$ > 400 nm), the ultraviolet-visible spectrum changes of 1,4-DHP solution under different photocatalysts. (A) AgBr/$Ti_3C_2$@$TiO_2$-40%, (B) AgBr, (C) $Ti_3C_2$@$TiO_2$ and (D) no catalyst.

The photocatalytic performance of the prepared AgBr/$Ti_3C_2$@$TiO_2$ composite was tested by the dehydrogenation of 1,4-DHP under visible light irradiation ($\lambda$ > 400 nm). As shown in Fig. 7A, the absorption peak of 1,4-DHP at 374 nm decreased rapidly, companying with the rapid increase at 280 nm. According to the previous literature, the simultaneous peak intensity decrease at 374 nm and increase at 280 nm indicates the dehydrogenation of 1,4-DHP,[53–55] namely the conversion of 1,4-DHP to its pyridine derivatives (Fig. 7A, inset). When AgBr and $Ti_3C_2$@$TiO_2$ were used as photocatalyst, the changes of the peak intensity at 374 and 280 nm were also observed, but the changes were much slower (Fig. 7B and C). When no catalyst was added and only irradiated under visible light, the changes of the two peaks were hardly observed. After 9 min irradiation under visible light, the conversion rate of 1,4-DHP were 98.9%, 84.5%, and 21.9% in the presence of AgBr/$Ti_3C_2$@$TiO_2$-40%, AgBr, and $Ti_3C_2$@$TiO_2$ respectively. The above results show that the as-prepared AgBr/$Ti_3C_2$@$TiO_2$ composites have much better photocatalytic performance for 1,4-DHP photodehydrogenation.

In order to further analyze the influence of $Ti_3C_2$@$TiO_2$ content on the photocatalytic properties of AgBr/$Ti_3C_2$@$TiO_2$ composites, we prepared a series of AgBr/$Ti_3C_2$@$TiO_2$ composites with different $Ti_3C_2$@$TiO_2$ content and evaluated their photocatalytic activities by the photodehydrogenation of 1,4-DHP. With the increase of $Ti_3C_2$@$TiO_2$ content, the photocatalytic performance of the AgBr/$Ti_3C_2$@$TiO_2$ composites first increased and then decreased. All of the composites displayed enhanced photocatalytic ability and the AgBr/$Ti_3C_2$@$TiO_2$-40% composite showed the highest photocatalytic activity (Fig. 8A and B). The rate constants of the photocatalyst for 1,4-DHP dehydrogenation are obtained by plotting $\ln(C/C_0)$ *versus* illumination time (Fig. 8C) and compared in Fig. 8D. The rate constant of AgBr/$Ti_3C_2$@$TiO_2$-40% (0.4044 $min^{-1}$) is the highest, which is about 3.9 times and 24.5 times as high as that of pure AgBr (0.1035 $min^{-1}$) and $Ti_3C_2$@$TiO_2$ (0.0165 $min^{-1}$), respectively, further confirming the enhanced photocatalytic ability of AgBr/$Ti_3C_2$@$TiO_2$ composites.

Besides the photodehydrogenation of 1,4-DHP, the AgBr/$Ti_3C_2$@$TiO_2$ composites was further applied for the photodegradation of TCH under visible light irradiation ($\lambda$ > 400 nm). As shown in Fig. 9A, when the catalyst is AgBr/$Ti_3C_2$@$TiO_2$-10%, the absorption peak of TCH at 357 nm decreases rapidly, indicating the efficient catalytic degradation of TCH. When AgBr and $Ti_3C_2$@$TiO_2$ were used as photocatalyst, the changes of the peak intensity at 357 nm were also observed, but the changes were much slower (Fig. 9B and C). No obvious changes could be observed without any catalyst (Fig. 9D). After 20 min irradiation under visible light, the degradation rate of TCH were 76.5%, 59.6%, and 31.9% in the presence of AgBr/$Ti_3C_2$@$TiO_2$-10%, AgBr, and $Ti_3C_2$@$TiO_2$, respectively. These results show that the photocatalytic performance of AgBr/$Ti_3C_2$@$TiO_2$-10% is much better than that of pure AgBr and $Ti_3C_2$@$TiO_2$.

Similarly, AgBr/$Ti_3C_2$@$TiO_2$ composites with different $Ti_3C_2$@$TiO_2$ contents were used to degrade TCH. With increase of $Ti_3C_2$@$TiO_2$ content, the photodegradation efficiency of AgBr/$Ti_3C_2$@$TiO_2$ composites increased first and then decreased. The

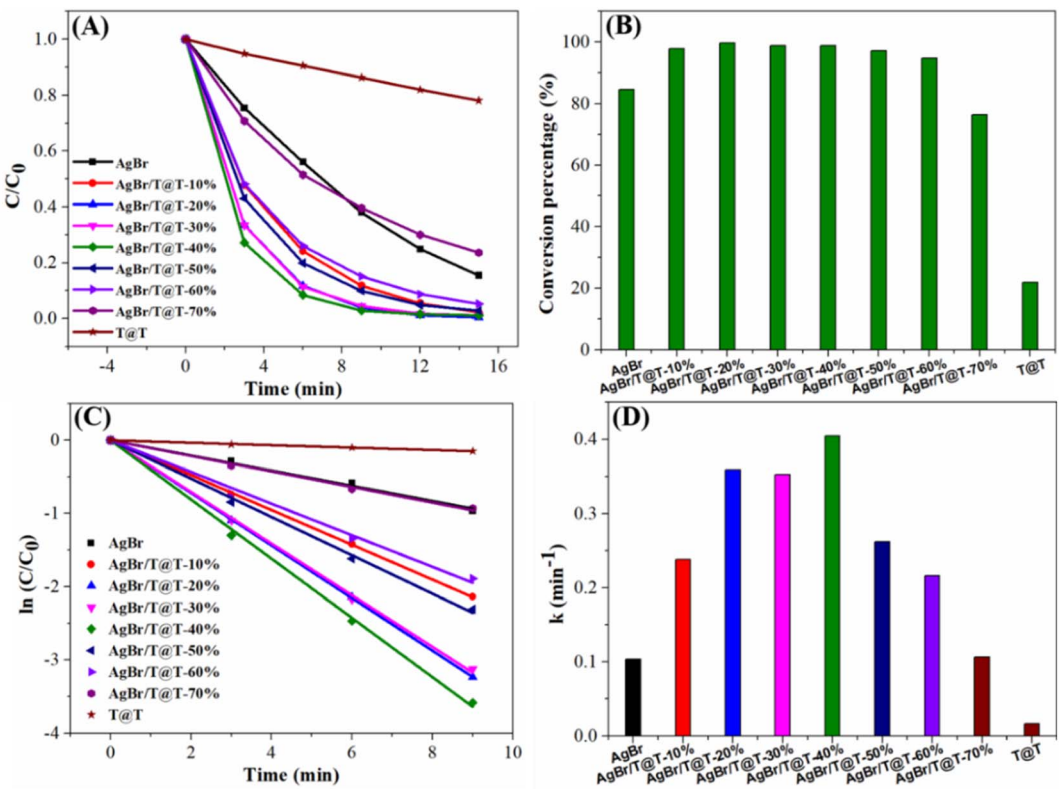


Fig. 8 AgBr, $Ti_3C_2$@$TiO_2$ (T@T for short) and AgBr/$Ti_3C_2$@$TiO_2$-*x*% (AgBr/T@T-*x*% for short) photocatalytic oxidation of 1,4-DHP under visible light: (A) kinetic diagram, (B) degradation efficiency graph, (C) the linear kinetic fitting graph, (D) apparent rate constant.

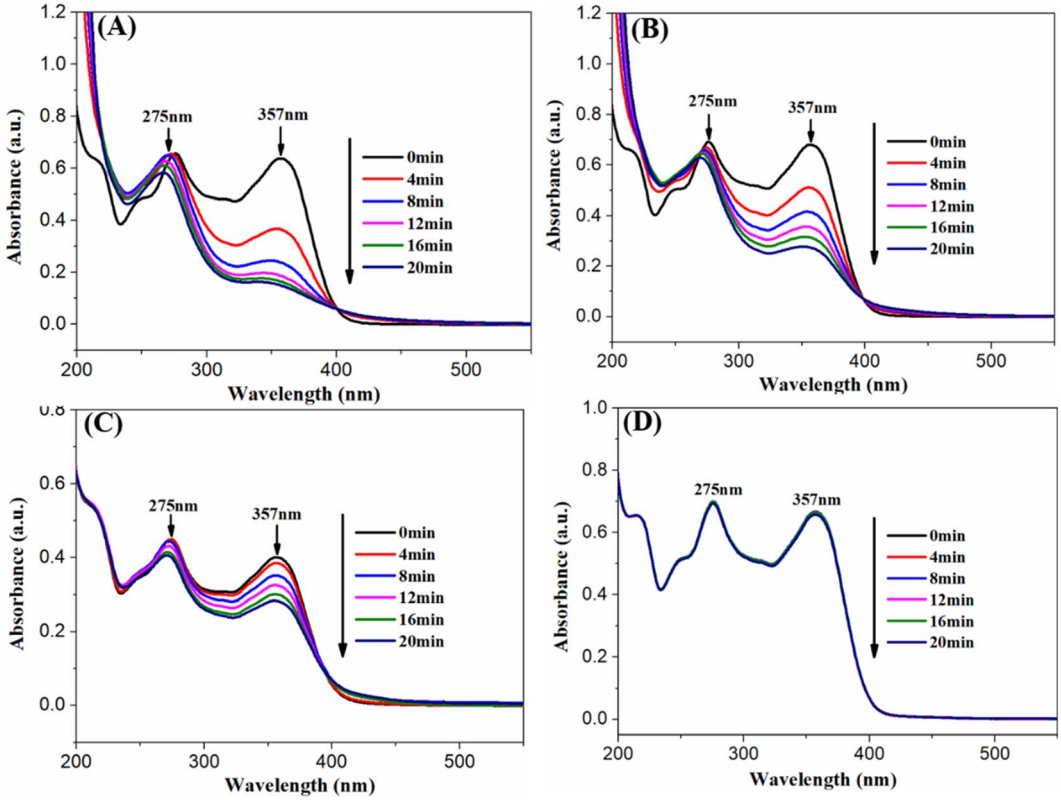


Fig. 9 Under the irradiation of visible light ($\lambda$ > 400 nm), the ultraviolet-visible spectrum changes of TCH solution under different photocatalysts. (A) AgBr/$Ti_3C_2$@$TiO_2$-10%, (B) AgBr, (C) $Ti_3C_2$@$TiO_2$ and (D) no catalyst.

photo-degradation results of TCH show that under visible light, the conversion rate of AgBr/$Ti_3C_2$@$TiO_2$-10% to TCH reaches 76.5% within 20 min, showing the highest photocatalytic activity (Fig. 10A and B). The photodegradation rate constant of TCH (Fig. 10D) is obtained by plotting $\ln(C/C_0)$ *vs.* time in Fig. 10C. Among them, the rate constant of AgBr/$Ti_3C_2$@$TiO_2$-10% is the highest (0.1027 $min^{-1}$), which is about 1.9 times and 5.9 times as high as that of pure AgBr (0.0540 $min^{-1}$) and $Ti_3C_2$@$TiO_2$ (0.0174 $min^{-1}$), respectively. The above data show that AgBr/$Ti_3C_2$@$TiO_2$ composite also has good photocatalytic performance for TCH degradation.

The UV-vis DRS spectra of the materials are shown in Fig. 11A. In comparison with pure AgBr, with an increase of $Ti_3C_2$@$TiO_2$ content, the light absorption ability of the composites gradually increases.[45,56] The fast charge transfer properties of the prepared materials were analyzed by PL spectroscopy. As shown in Fig. 11B, compared with the pure AgBr, pure $Ti_3C_2$ and $Ti_3C_2$@$TiO_2$ samples, the emission peaks of the AgBr/$Ti_3C_2$@$TiO_2$ composite are of weaker intensity, indicating the beneficial effect of the heterojunction to promote the separation efficiency of photo-induced electron–hole pairs.[35,57] Electrochemical impedance spectroscopy (EIS) tests is used to study the electrochemical performance. Fig. 11C shows the Nyquist diagram of EIS of AgBr, $Ti_3C_2$@$TiO_2$ and AgBr/$Ti_3C_2$@$TiO_2$ photocatalysts. In general, the arc radius in the Nyquist diagram describes the reaction rate at the electrode surface, the smaller the radius, the lower the corresponding electron transfer resistance, the higher the charge transfer and separation efficiency.[58] The arc radii of AgBr/$Ti_3C_2$@$TiO_2$ composites are much smaller than that of pure AgBr and $Ti_3C_2$@$TiO_2$, which indicates that more efficient photogenerated charge carrier's separation, lower internal resistance and faster transfer of charge carriers can occur on the surface of AgBr/$Ti_3C_2$@$TiO_2$ composites. These results demonstrate that AgBr is successfully compounded with $Ti_3C_2$@$TiO_2$ and has good photogenerated charge carrier separation efficiency. Fig. 11D–F shows the Mott–Schottky curves of AgBr, $Ti_3C_2$@$TiO_2$ and AgBr/$Ti_3C_2$@$TiO_2$-10% materials. As can be seen from the figure that AgBr is considered as an n-type semiconductor because of its positive slope (Fig. 11D). Although $TiO_2$ is also an n-type semiconductor,[59] its Mott–Schottky diagram slope of $Ti_3C_2$@$TiO_2$ composite material is negative after *in situ* growth on $Ti_3C_2$ by solvothermal method, and it has the potential of a p-type semiconductor[2,23] (Fig. 11E). More importantly, the Mott–Schottky diagram of AgBr/$Ti_3C_2$@$TiO_2$-10% composite shows an inverted "V-shape" as shown in Fig. 11F, which indicates that the p–n junction structure has been successfully formed.

Using AgBr/$Ti_3C_2$@$TiO_2$ composite catalyst, four repeated experiments were carried out to determine the photodehydrogenation of 1,4-DHP and the photodegradation of TCH separately to evaluate the stability of the prepared photocatalyst. After four cycles, the relative hydrogenation efficiency of 1,4-DHP was 86.2% (Fig. 12A and B), and the relative degradation efficiency of TCH was 93.8% (Fig. 12C and D). Part of the

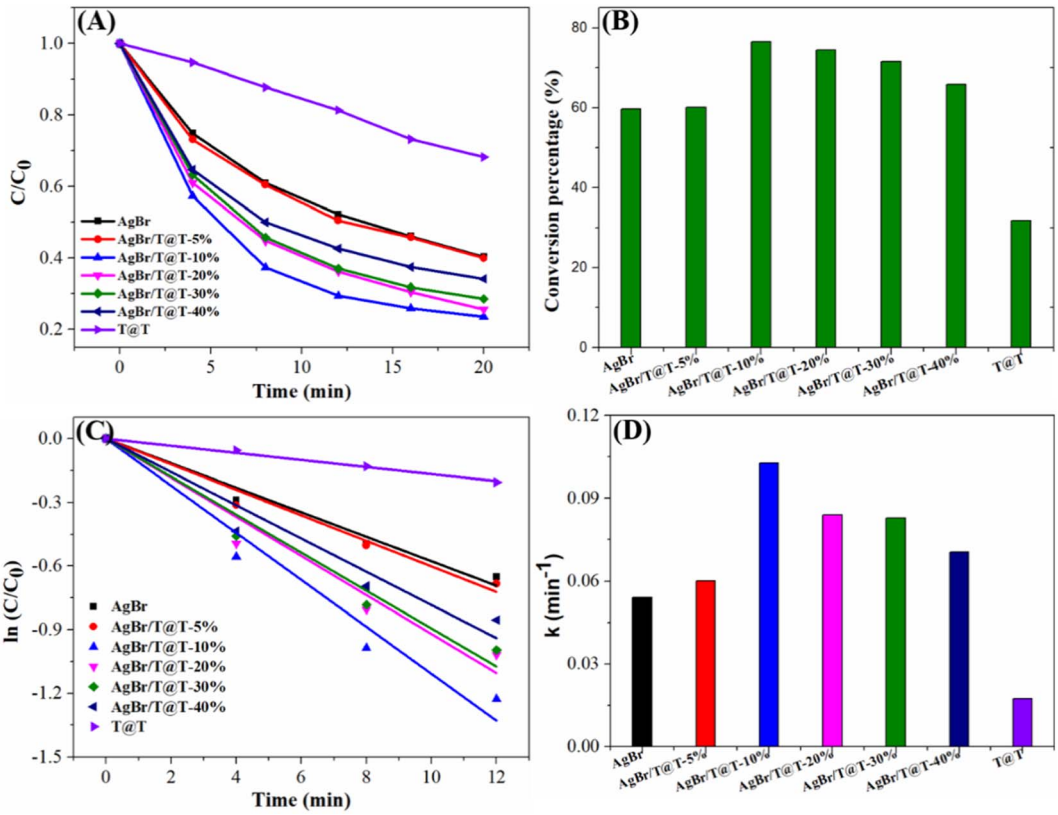


Fig. 10 AgBr, $Ti_3C_2$@$TiO_2$ (T@T for short) and AgBr/$Ti_3C_2$@$TiO_2$-*x*% (AgBr/T@T-*x*% for short) photocatalytic degradation of TCH under visible light: (A) kinetic diagram, (B) degradation efficiency graph, (C) the linear kinetic fitting graph, (D) apparent rate constant.

reason for the decrease in efficiency may be due to the loss of the catalyst during the cycle. Therefore, AgBr/$Ti_3C_2$@$TiO_2$ composite has good photocatalytic stability and potential practical application.

Active species capture experiment was conducted to explore the three main active species in photocatalytic reaction,[60] ammonium oxalate (AO), benzoquinone (BQ) and isopropanol (IPA) were used as scavengers for $h^+$, $^{\cdot}O_2^-$ and $^{\cdot}OH$, respectively.[53] As shown in Fig. 13, the addition of IPA slightly decreased the degradation of TCH but has little effect on the dehydrogenation of 1,4-DHP, the addition of AO has a little effect on the degradation of TCH, but slightly decreased the dehydrogenation of 1,4-DHP. When BQ was added to the reaction system, the degradation of TCH was obviously inhibited (Fig. 13A), indicating the major role of $^{\cdot}O_2^-$ in TCH degradation. The addition of BQ has significant influence on absorption spectrum of 1,4-DHP (data not shown), so BQ is not suitable for the detection of $^{\cdot}O_2^-$ radicals in the reaction system of 1,4-DHP. It was generally thought that the dissolved oxygen ($O_2$) in the reaction solution accepted photo-excited electrons from the conduction band of a semiconductor to produced $^{\cdot}O_2^-$ ($O_2 + e^- \rightarrow {}^{\cdot}O_2^-$).[61] Therefore, the removal of $O_2$ from the 1,4-DHP reaction system would affect the photodehydrogenation of 1,4-DHP, if $^{\cdot}O_2^-$ was involved in the dehydrogenation process. With this in mind, we carried out the photodehydrogenation of 1,4-DHP under a nitrogen atmosphere. The dissolved $O_2$ was removed from the reaction by nitrogen bubbling. The removal of $O_2$ apparently suppressed the dehydrogenation of 1,4-DHP (Fig. 13B). This results suggested that $^{\cdot}O_2^-$ was also played important role in 1,4-DHP dehydrogenation, just as in TCH degradation.

EPR technique was employed to further detect the generation of $^{\cdot}O_2^-$ in the AgBr/$Ti_3C_2$@$TiO_2$ composite involved photocatalytic system. DMPO was used as a radical trap. As shown in Fig. 13C, the DMPO-$^{\cdot}O_2^-$ characteristic peak was observed under visible light irradiation,[62] but not observed in dark condition. The production of $^{\cdot}OH$ by AgBr/$Ti_3C_2$@$TiO_2$ composite during the photocatalysis process was probed by fluorescence technique.[63] The fluorescence absorption peak around 425 nm obviously increased with visible-light irradiation time (Fig. 13D), indicating the formation of hydroxyl terephthalic acid (TA-OH), confirmed the generation of $^{\cdot}OH$ on the surface of AgBr/$Ti_3C_2$@$TiO_2$ composites.[53]

According to the results of active species capture experiment, EPR trapping experiment and terephthalic acid-based fluorescence experiment, a possible photocatalytic reaction mechanism was proposed (Fig. 14).

Under the excitation of visible light, AgBr with narrow band gap (2.6 eV) absorbs photons and produces photogenerated electron–hole pairs (eqn (1)). According to theoretical analysis, the conduction band (CB) potential of AgBr is more negative than the CB potential of $TiO_2$ and the Fermi

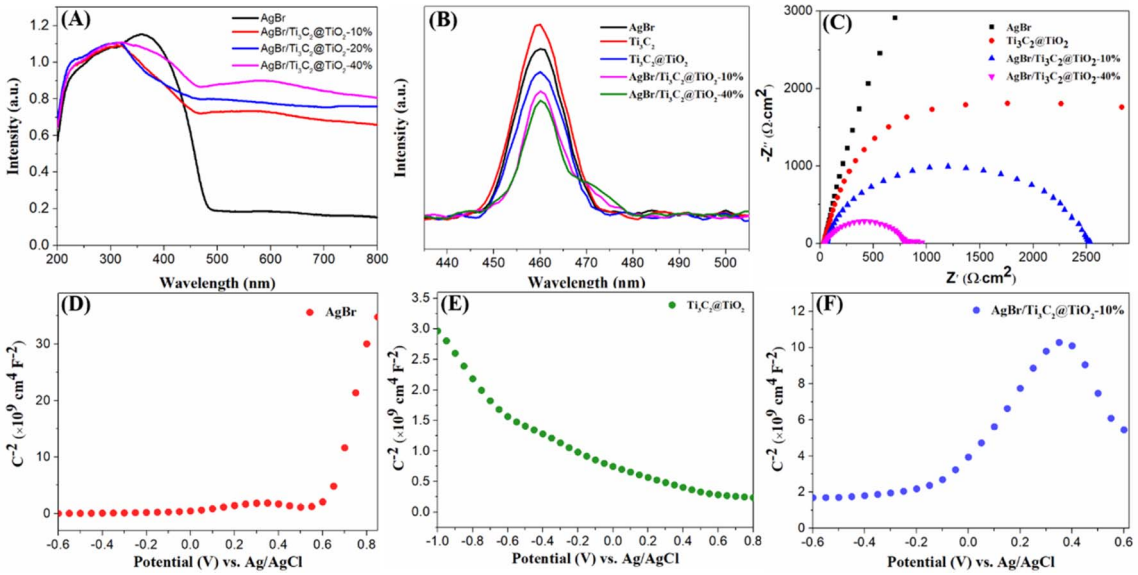


Fig. 11 UV-vis DRS of the as-prepared samples (A), PL spectra (B), EIS Nyquist plots of samples (C), Mott–Schottky plots of AgBr (D), $Ti_3C_2$@$TiO_2$ (E) and AgBr/$Ti_3C_2$@$TiO_2$-10% (F).

level of $Ag^0$ nanoparticles.[64–66] Therefore, the electrons on the CB of AgBr can rapidly transfer to the CB of $TiO_2$ (eqn (2)) or be captured by $Ag^0$ nanoparticles through Schottky barrier (eqn (3)).[67] The electrons on the CB of $TiO_2$ can further transfer to $Ti_3C_2$ (eqn (4)), since the CB potentials of $TiO_2$ is more negative than the Fermi level of the $Ti_3C_2$.[30,68,69] Thus, the photoinduced charge carriers on AgBr is efficiently separated, and the photocatalytic activity of AgBr is improved by

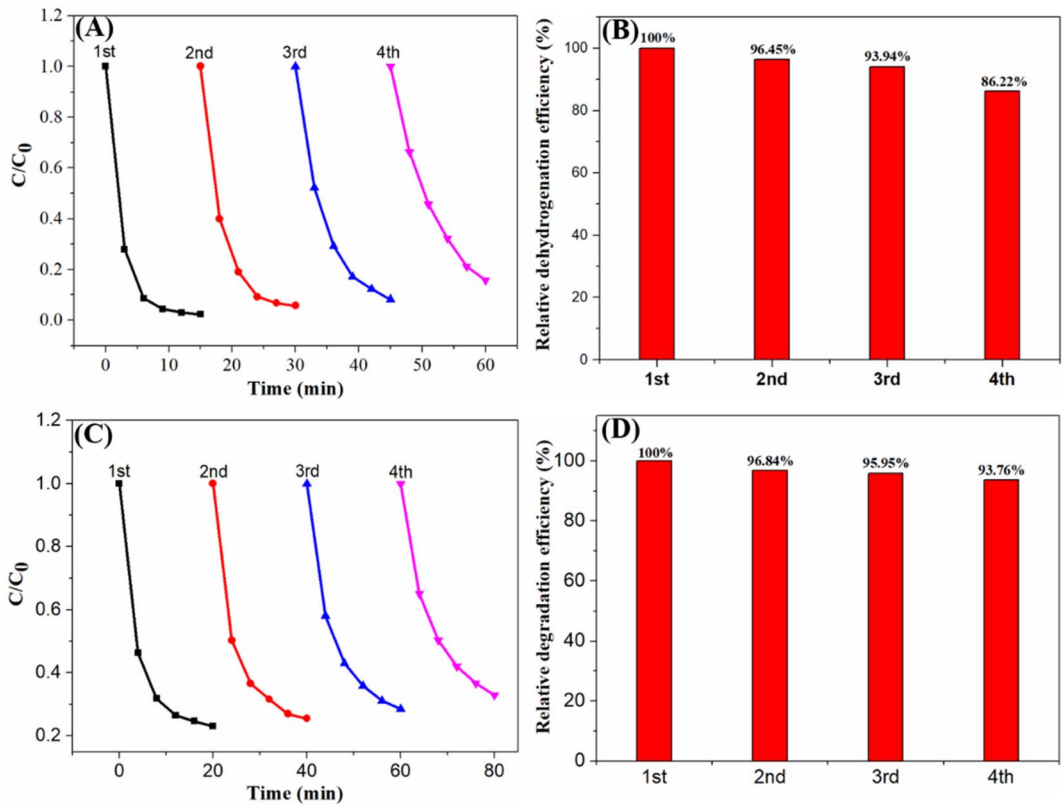


Fig. 12 Cyclic kinetics curve and relative dehydrogenation efficiency of 1,4-DHP by AgBr/$Ti_3C_2$@$TiO_2$-40% (A and B); cyclic kinetics curve and relative degradation efficiency of TCH by AgBr/$Ti_3C_2$@$TiO_2$-10% (C and D).

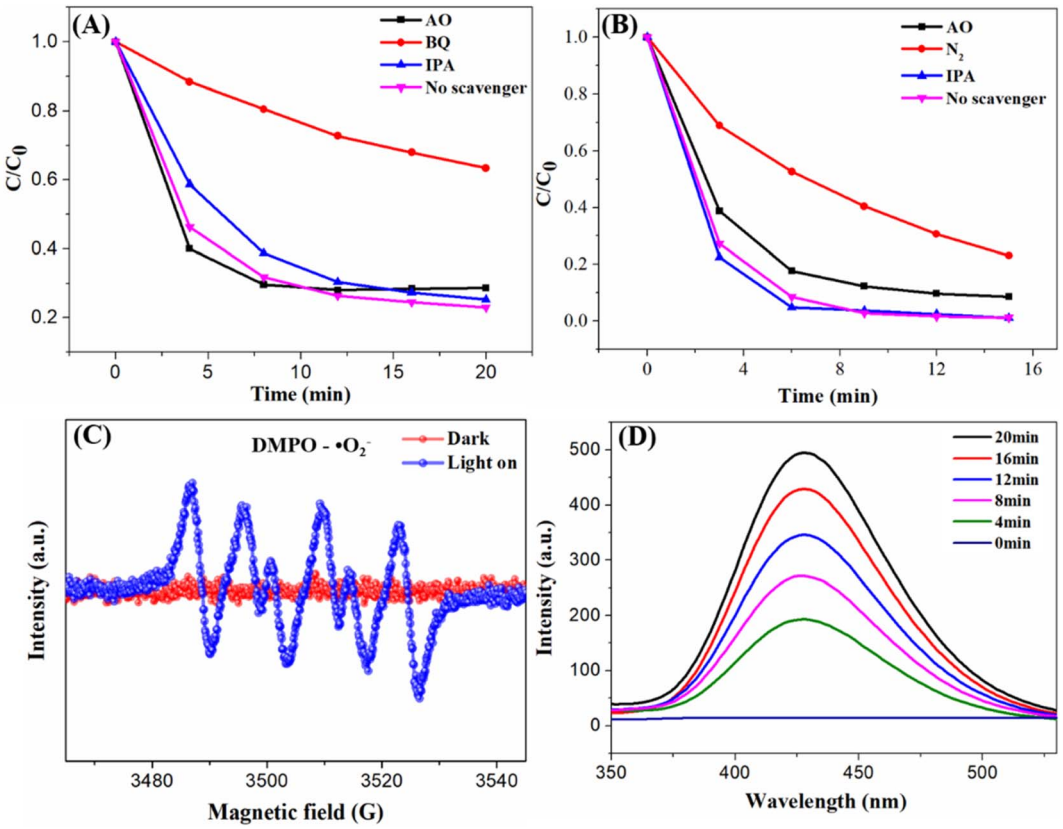


Fig. 13 The effect of certain selected scavengers on the photooxidation of TCH (A) and 1,4-DHP (B) under visible light ($\lambda > 400$ nm) irradiation, EPR signals of AgBr/$Ti_3C_2$@$TiO_2$ under dark and visible light irradiation (C) and fluorescence spectra of 0.5 mM alkaline terephthalic acid (TA) solution in the presence of AgBr/$Ti_3C_2$@$TiO_2$ composite under visible light irradiation (D).

compositing with $Ti_3C_2$@$TiO_2$. The electrons transferred to $Ag^0$ and $Ti_3C_2$ are subsequently captured by $O_2$ to produce $^{\cdot}O_2^-$ (eqn (5) and (6)). At the same time, the $h^+$ left on the valence band (VB) of AgBr can convert $H_2O$ and $OH^-$ ($H_2O$/$OH^-$) to $^{\cdot}OH$ (eqn (7)). The produced $^{\cdot}O_2^-$, $^{\cdot}OH$ and $h^+$ may all be utilized as oxidizer for 1,4-DHP dehydrogenation and TCH degradation (eqn (8)).

$$AgBr + h\nu \rightarrow AgBr\ (e^- + h^+) \quad (1)$$

$$AgBr\ (e^-) + TiO_2 \rightarrow AgBr + TiO_2\ (e^-) \quad (2)$$

$$AgBr\ (e^-) + Ag^0 \rightarrow AgBr + Ag^0\ (e^-) \quad (3)$$

$$TiO_2\ (e^-) + Ti_3C_2 \rightarrow TiO_2 + Ti_3C_2\ (e^-) \quad (4)$$

$$Ag^0\ (e^-) + O_2 \rightarrow {}^{\cdot}O_2^- + Ag^0 \quad (5)$$

$$Ti_3C_2\ (e^-) + O_2 \rightarrow {}^{\cdot}O_2^- + Ti_3C_2 \quad (6)$$

$$AgBr\ (h^+) + H_2O/OH^- \rightarrow {}^{\cdot}OH + AgBr \quad (7)$$

$$^{\cdot}O_2^-, {}^{\cdot}OH, h^+ + \text{1,4-DHP/TCH} \rightarrow \text{products} \quad (8)$$

It is worth pointing out that the main active species are $^{\cdot}O_2^-$ and $h^+$ for 1,4-DHP dehydrogenation, while $^{\cdot}O_2^-$ and $^{\cdot}OH$ for TCH degradation. In other words, the photogenerated $h^+$ in the VB of AgBr can react with $H_2O$ and $OH^-$ to produce $^{\cdot}OH$, then the generated $^{\cdot}OH$ is consumed by the oxidation of TCH in the TCH-catalyst system. But for the 1,4-DHP-catalyst system, the generated $^{\cdot}OH$ cannot be consumed by 1,4-DHP, which will influence the separation of photogenerated electron–hole pairs. The transfer of electrons in the CB of AgBr to separate it from the photogenerated holes in the VB of AgBr is more urgent in the 1,4-DHP-catalysts system. Therefore, the introduction of $Ti_3C_2$@$TiO_2$ into AgBr is more pronounced to enhance the catalytic activity of AgBr for 1,4-DHP oxidation. This maybe also one of the reasons that the optimal proportion of $Ti_3C_2$@$TiO_2$ is different for 1,4-DHP and TCH.

To sum up, under visible light irradiation, The enhanced photocatalytic performance of AgBr/$Ti_3C_2$@$TiO_2$ composite should be attributed to the following aspects: (1) the formation of a p–n heterojunction between AgBr and $TiO_2$ and the introduction of $Ti_3C_2$ as an electron transport medium and acceptor can rapidly transfer electrons, thus enhancing the separation rate of photo-generated electron–hole pairs; (2) as the size of AgBr particles in the composite decreases, the specific surface area of the composite increases, and the contact area between the interfaces of AgBr, $TiO_2$ and $Ti_3C_2$ increases, which also promotes the transfer of photogenerated carriers. (3) $Ti_3C_2$ and AgBr has good absorption capacity for visible light, which can increase the utilization of visible light by composite materials.

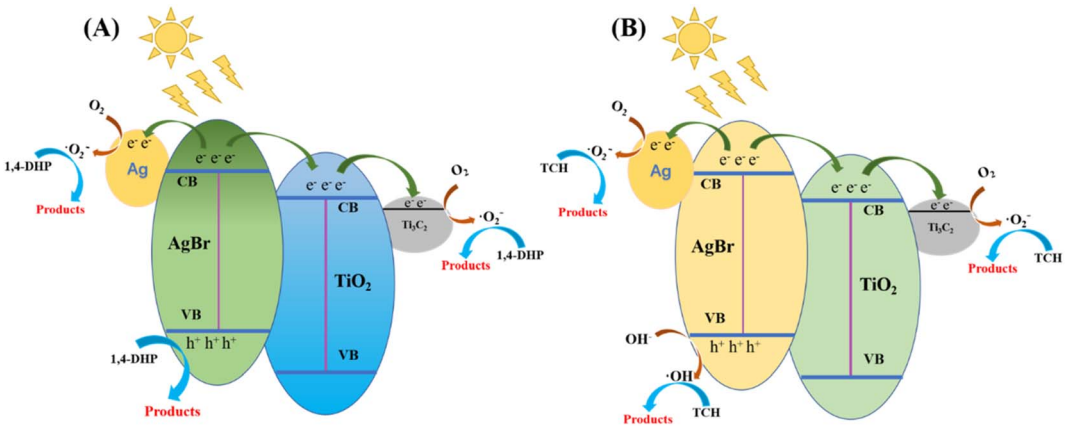


Fig. 14 Hypothetical mechanism diagram of dehydrogenation of 1,4-DHP (A) and photodegradation of TCH (B) by AgBr/$Ti_3C_2$@$TiO_2$ composites under visible light ($\lambda$ > 400 nm).

## 4. Conclusions

In conclusion, AgBr/$Ti_3C_2$@$TiO_2$ composite photocatalyst was prepared by solvothermal and precipitation method and the photocatalytic performance of the composite was evaluated by the photodehydrogenation of 1,4-DHP and photodegradation of TCH under visible light irradiation. The AgBr/$Ti_3C_2$@$TiO_2$ composite photocatalyst showed improved photocatalytic performance compared with AgBr and $Ti_3C_2$@$TiO_2$. The photocatalytic performance of the AgBr/$Ti_3C_2$@$TiO_2$ composite with optimized composition is 3.9 and 24.5 times higher than that of pure AgBr and $Ti_3C_2$@$TiO_2$, respectively, for photodehydrogenation of 1,4-DHP and 1.9 and 5.9 times higher than that of pure AgBr and $Ti_3C_2$@$TiO_2$ for photodegradation of TCH. The improvement of photocatalytic performance of AgBr/$Ti_3C_2$@$TiO_2$ composite is due to the formation of p–n heterojunction structure between AgBr and $Ti_3C_2$@$TiO_2$, and the using of $Ti_3C_2$ as cocatalyst, which reduced the internal resistance, accelerated charge transfer and improved the separation efficiency of photogenerated carriers. In addition, AgBr/$Ti_3C_2$@$TiO_2$ composite photocatalyst also showed good stability in photochemical reaction, indicating that the AgBr/$Ti_3C_2$@$TiO_2$ composite has potential application in photooxidation reaction, wastewater treatment and environmental remediation.

## Conflicts of interest

There are no conflicts of interest to declare.

## Acknowledgements

This work was supported by the Opening Project of Key Laboratory of Green Chemistry of Sichuan Institutes of Higher Education (LZJ2002) and the Open Project of Chemical Synthesis and Pollution Control Key Laboratory of Sichuan Province (CSPC2016-3-2).

## References

1 X. Shi, B. Ren, X. Jin, X. C. Wang and P. Jin, Metabolic hazards of pharmaceuticals and personal care products (PPCPs) in sewers, *J. Hazard. Mater.*, 2022, **432**, 128539.
2 S. Li, Y. Wang, J. Wang, J. Liang, Y. Li and P. Li, Modifying g-$C_3N_4$ with oxidized $Ti_3C_2$ MXene for boosting photocatalytic U(VI) reduction performance, *J. Mol. Liq.*, 2022, **346**, 117937.
3 P. Zhang, J. Xu, X.-J. Wang, B. He, S.-Q. Gao and Y.-W. Lin, The Third Generation of Artificial Dye-Decolorizing Peroxidase Rationally Designed in Myoglobin, *ACS Catal.*, 2019, **9**, 7888–7893.
4 D. Ren, R. Shen, Z. Jiang, X. Lu and X. Li, Highly efficient visible-light photocatalytic $H_2$ evolution over 2D-2D CdS/$Cu_7S_4$ layered heterojunctions, *Chin. J. Catal.*, 2020, **41**, 31–40.
5 C. Bie, H. Yu, B. Cheng, W. Ho, J. Fan and J. Yu, Design, Fabrication, and Mechanism of Nitrogen-Doped Graphene-Based Photocatalyst, *Adv. Mater.*, 2021, **33**, 2003521.
6 X. Bao, D. Lu, Z. Wang, H. Yin, B. Zhu, B. Chen, M. Shi, Y. Zhang, Q. Xu, Y. Qin, X. C. Shen and K. Wu, Significantly enhanced photothermal catalytic $CO_2$ reduction over $TiO_2$/g-$C_3N_4$ composite with full spectrum solar light, *J. Colloid Interface Sci.*, 2023, **638**, 63–75.
7 M. Tian, J. Wang, R. Sun, D. Lu, N. Li, T. Liu, M. Yao, G. Zhang and L. Li, Facile synthesis of rod-like $TiO_2$-based composite loaded with g-$C_3N_4$ for efficient removal of high-chroma organic pollutants based on adsorption-photocatalysis mechanism, *Inorg. Chem. Commun.*, 2022, **141**, 109517.
8 Y. Elviera, D. O. B. Yulizar, R. Apriandanu and S. Marcony, Fabrication of novel $SnWO_4$/ZnO using Muntingia calabura L. leaf extract with enhanced photocatalytic methylene blue degradation under visible light irradiation, *Ceram. Int.*, 2022, **48**, 3564–3577.
9 P. Hemmatpour and A. Nezamzadeh-Ejhieh, A Z-scheme CdS/$BiVO_4$ photocatalysis towards Eriochrome black T: An experimental design and mechanism study, *Chemosphere*, 2022, **307**, 135925.

10 H. Lu, Y. Liu, S. Zhang, J. Wan, X. Wang, L. Deng, J. Kan and G. Wu, Clustered tubular S-scheme ZnO/CdS heterojunctions for enhanced photocatalytic hydrogen production, *Mater. Sci. Eng., B*, 2023, **289**, 116282.

11 T. Ren, Y. Dang, Y. Xiao, Q. Hu, D. Deng, J. Chen and P. He, Depositing Ag nanoparticles on g-$C_3N_4$ by facile silver mirror reaction for enhanced photocatalytic hydrogen production, *Inorg. Chem. Commun.*, 2021, **123**, 108367.

12 F. Dong, Z. Wang, Y. Li, W. K. Ho and S. C. Lee, Immobilization of polymeric g-$C_3N_4$ on structured ceramic foam for efficient visible light photocatalytic air purification with real indoor illumination, *Environ. Sci. Technol.*, 2014, **48**, 10345–10353.

13 Z. Miao, G. Wang, X. Zhang and X. Dong, Oxygen vacancies modified $TiO_2$/$Ti_3C_2$ derived from MXenes for enhanced photocatalytic degradation of organic pollutants: The crucial role of oxygen vacancy to Schottky junction, *Appl. Surf. Sci.*, 2020, **528**, 146929.

14 Y. Yan, X. Zhou, P. Yu, Z. Li and T. Zheng, Characteristics, mechanisms and bacteria behavior of photocatalysis with a solid Z-scheme Ag/AgBr/g-$C_3N_4$ nanosheet in water disinfection, *Appl. Catal., A*, 2020, **590**, 117282.

15 A. Ren, C. Liu, Y. Hong, W. Shi, S. Lin and P. Li, Enhanced visible-light-driven photocatalytic activity for antibiotic degradation using magnetic $NiFe_2O_4$/$Bi_2O_3$ heterostructures, *Chem. Eng. J.*, 2014, **258**, 301–308.

16 Y. Shi, Z. Yan, Y. Xu, T. Tian, J. Zhang, J. Pang, X. Peng, Q. Zhang, M. Shao, W. Tan, H. Li and Q. Xiong, Visible-light-driven AgBr–$TiO_2$-Palygorskite photocatalyst with excellent photocatalytic activity for tetracycline hydrochloride, *J. Cleaner Prod.*, 2020, **277**, 124021.

17 P. Laokul, N. Kanjana, R. Ratchatanee, S. Ruangjan, N. Kotsarn, A. Chingsungnoen and P. Poolcharuansin, Preparation of AgBr decorated ZnO/ZnS nanocomposite for photocatalytic and antibacterial applications, *Mater. Chem. Phys.*, 2023, **295**, 127112.

18 X. Xue, X. Chen, Z. Zhang, G. Fan and T. Ma, Improved ionic organic pollutant degradation under visible light by Ag SPR-promoted phosphorus-doped g-$C_3N_4$/AgBr/$Bi_2WO_6$ with excellent charge transfer capacity and high surface area, *J. Alloys Compd.*, 2023, **930**, 167457.

19 W. Wang, L. Jing, Y. Qu, Y. Luan, H. Fu and Y. Xiao, Facile fabrication of efficient AgBr-$TiO_2$ nanoheterostructured photocatalyst for degrading pollutants and its photogenerated charge transfer mechanism, *J. Hazard. Mater.*, 2012, **243**, 169–178.

20 K. Dai, J. Lv, L. Lu, Q. Liu, G. Zhu and D. Li, Synthesis of micro-nano heterostructure AgBr/ZnO composite for advanced visible light photocatalysis, *Mater. Lett.*, 2014, **130**, 5–8.

21 P. Singh, Sonu, P. Raizada, A. Sudhaik, P. Shandilya, P. Thakur, S. Agarwal and V. K. Gupta, Enhanced photocatalytic activity and stability of AgBr/BiOBr/graphene heterojunction for phenol degradation under visible light, *J. Saudi Chem. Soc.*, 2019, **23**, 586–599.

22 M. Abou Asi, C. He, M. Su, D. Xia, L. Lin, H. Deng, Y. Xiong, R. Qiu and X.-Z. Li, Photocatalytic reduction of $CO_2$ to hydrocarbons using AgBr/$TiO_2$ nanocomposites under visible light, *Catal. Today*, 2011, **175**, 256–263.

23 Y. Cui, Z. Zhang, B. Li, R. Guo, X. Zhang, X. Cheng, M. Xie and Q. Cheng, Ultrasound assisted fabrication of AgBr/$TiO_2$ nano-tube arrays photoelectrode and its enhanced visible photocatalytic performance and mechanism for detoxification of 4-chlorophenol, *Sep. Purif. Technol.*, 2018, **197**, 189–196.

24 M. Naguib, M. Kurtoglu, V. Presser, J. Lu, J. Niu, M. Heon, L. Hultman, Y. Gogotsi and M. W. Barsoum, Two-dimensional nanocrystals produced by exfoliation of $Ti_3AlC_2$, *Adv. Mater.*, 2011, **23**, 4248–4253.

25 R. Zhao, M. Wang, D. Zhao, H. Li, C. Wang and L. Yin, Molecular-Level Heterostructures Assembled from Titanium Carbide MXene and Ni–Co–Al Layered Double-Hydroxide Nanosheets for All-Solid-State Flexible Asymmetric High-Energy Supercapacitors, *ACS Energy Lett.*, 2017, **3**, 132–140.

26 Y. Yang, D. Zhang and Q. Xiang, Plasma-modified $Ti_3C_2T_x$/CdS hybrids with oxygen-containing groups for high-efficiency photocatalytic hydrogen production, *Nanoscale*, 2019, **11**, 18797–18805.

27 M. Wu, M. He, Q. Hu, Q. Wu, G. Sun, L. Xie, Z. Zhang, Z. Zhu and A. Zhou, $Ti_3C_2$ MXene-Based Sensors with High Selectivity for $NH_3$ Detection at Room Temperature, *ACS Sens.*, 2019, **4**, 2763–2770.

28 J. Guo, Q. Peng, H. Fu, G. Zou and Q. Zhang, Heavy-Metal Adsorption Behavior of Two-Dimensional Alkalization-Intercalated MXene by First-Principles Calculations, *J. Phys. Chem. C*, 2015, **119**, 20923–20930.

29 C. Cai, R. Wang, S. Liu, X. Yan, L. Zhang, M. Wang, Q. Tong and T. Jiao, Synthesis of self-assembled phytic acid-MXene nanocomposites *via* a facile hydrothermal approach with elevated dye adsorption capacities, *Colloids Surf., A*, 2020, **589**, 124468.

30 J. Low, L. Zhang, T. Tong, B. Shen and J. Yu, $TiO_2$/MXene $Ti_3C_2$ composite with excellent photocatalytic $CO_2$ reduction activity, *J. Catal.*, 2018, **361**, 255–266.

31 Z. Liu, Y. Zhou, L. Yang and R. Yang, Green preparation of *in situ* oxidized $TiO_2$/$Ti_3C_2$ heterostructure for photocatalytic hydrogen production, *Adv. Powder Technol.*, 2021, **32**, 4857–4861.

32 B. Tan, Y. Fang, Q. Chen, X. Ao and Y. Cao, Construction of $Bi_2O_2CO_3$/$Ti_3C_2$ heterojunctions for enhancing the visible-light photocatalytic activity of tetracycline degradation, *J. Colloid Interface Sci.*, 2021, **601**, 581–593.

33 B. Sun, F. Tao, Z. Huang, W. Yan, Y. Zhang, X. Dong, Y. Wu and G. Zhou, $Ti_3C_2$ MXene-bridged Ag/$Ag_3PO_4$ hybrids toward enhanced visible-light-driven photocatalytic activity, *Appl. Surf. Sci.*, 2021, **535**, 147354.

34 Y. Cao, L. Yue, Z. Li, Y. Han, J. Lian, H. Qin and S. He, Construction of Sn-Bi-MOF/$Ti_3C_2$ Schottky junction for photocatalysis of tetracycline: Performance and degradation mechanism, *Appl. Surf. Sci.*, 2023, **609**, 155191.

35 H. Wang, R. Zhao, J. Qin, H. Hu, X. Fan, X. Cao and D. Wang, MIL-100(Fe)/$Ti_3C_2$ MXene as a Schottky Catalyst with

Enhanced Photocatalytic Oxidation for Nitrogen Fixation Activities, *ACS Appl. Mater. Interfaces*, 2019, **11**, 44249–44262.
36 Y. Li, X. Deng, J. Tian, Z. Liang and H. Cui, $Ti_3C_2$ MXene-derived $Ti_3C_2/TiO_2$ nanoflowers for noble-metal-free photocatalytic overall water splitting, *Appl. Mater. Today*, 2018, **13**, 217–227.
37 J. Shu, Z. Wang, G. Xia, Y. Zheng, L. Yang and W. Zhang, One-pot synthesis of AgCl@Ag hybrid photocatalyst with high photocatalytic activity and photostability under visible light and sunlight irradiation, *Chem. Eng. J.*, 2014, **252**, 374–381.
38 G. Zou, Z. Zhang, J. Guo, B. Liu, Q. Zhang, C. Fernandez and Q. Peng, Synthesis of MXene/Ag Composites for Extraordinary Long Cycle Lifetime Lithium Storage at High Rates, *ACS Appl. Mater. Interfaces*, 2016, **8**, 22280–22286.
39 C. Xu, D. Li, H. Liu, D. Wang, X. Liu, S. Lin, Y. Yang, D. Fan and H. Pan, Construction of 1D/0D CdS nanorods/$Ti_3C_2$ QDs Schottky heterojunctions for efficient photocatalysis, *J. Environ. Chem. Eng.*, 2023, **11**, 109191.
40 Y. Wang, X. Wang, Y. Ji, R. Bian, J. Li, X. Zhang, J. Tian, Q. Yang and F. Shi, $Ti_3C_2$ MXene coupled with CdS nanoflowers as 2D/3D heterostructures for enhanced photocatalytic hydrogen production activity, *Int. J. Hydrogen Energy*, 2022, **47**, 22045–22053.
41 H. Liu, C. Yang, X. Jin, J. Zhong and J. Li, One-pot hydrothermal synthesis of MXene $Ti_3C_2/TiO_2$/BiOCl ternary heterojunctions with improved separation of photoactivated carries and photocatalytic behavior toward elimination of contaminants, *Colloids Surf., A*, 2020, **603**, 125239.
42 X. Liu, D. Zhang, B. Guo, Y. Qu, G. Tian, H. Yue and S. Feng, Recyclable and visible light sensitive Ag–AgBr/$TiO_2$: Surface adsorption and photodegradation of MO, *Appl. Surf. Sci.*, 2015, **353**, 913–923.
43 K. Huang, C. Lv, C. Li, H. Bai and X. Meng, $Ti_3C_2$ MXene supporting platinum nanoparticles as rapid electrons transfer channel and active sites for boosted photocatalytic water splitting over g-$C_3N_4$, *J. Colloid Interface Sci.*, 2023, **636**, 21–32.
44 W. Li, H. Chen, Y. Liu, T. Cai, W. Dong and X. Xia, A novel $Ti_3C_2$ MXene/PDI supramolecules composite with enhanced photocatalytic activities for degradation of tetracycline hydrochloride under visible-light, *J. Environ. Chem. Eng.*, 2022, **10**, 107978.
45 B. Saini, K. Harikrishna, D. Laishram, R. Krishnapriya, R. Singhal and R. K. Sharma, Role of ZnO in ZnO Nanoflake/$Ti_3C_2$ MXene Composites in Photocatalytic and Electrocatalytic Hydrogen Evolution, *ACS Appl. Nano Mater.*, 2022, **5**, 9319–9333.
46 D. Chen, M. Liu, Q. Chen, L. Ge, B. Fan, H. Wang, H. Lu, D. Yang, R. Zhang, Q. Yan, G. Shao, J. Sun and L. Gao, Large-scale synthesis and enhanced visible-light-driven photocatalytic performance of hierarchical Ag/AgCl nanocrystals derived from freeze-dried PVP-$Ag^+$ hybrid precursors with porosity, *Appl. Catal., B*, 2014, **144**, 394–407.
47 Z. Zhang, J. Yu, L. Ma, Y. Sun, P. Wang, T. Wang and S. Peng, Preparation of the plasmonic Ag/AgBr/ZnO film substrate for reusable SERS detection: Implication to the Z-scheme photocatalytic mechanism, *Spectrochim. Acta, Part A*, 2020, **224**, 117381.
48 X. Peng, J. Tian, S. Zhang, W. Xiao, X. Tian, Y. Wang, J. Xue and D. Lei, Z-scheme transfer pathway assisted photoelectrocatalyst $Zn_2SnO_4$/rGO/Ag/AgBr for organic pollutants treatment, *Colloids Surf., A*, 2023, **657**, 130552.
49 L. Xiu, Z. Wang, M. Yu, X. Wu and J. Qiu, Aggregation-resistant 3D MXene-based architecture as efficient bifunctional electrocatalyst for overall water splitting, *ACS Nano*, 2018, **12**, 8017–8028.
50 N. Liu, N. Lu, H. Yu, S. Chen and X. Quan, Efficient day-night photocatalysis performance of 2D/2D $Ti_3C_2$/porous g-$C_3N_4$ nanolayers composite and its application in the degradation of organic pollutants, *Chemosphere*, 2020, **246**, 125760.
51 Z. Mao, W. Hao, W. Wang, F. Ma, C. Ma and S. Chen, BiOI@$CeO_2$@$Ti_3C_2$ MXene composite S-scheme photocatalyst with excellent bacteriostatic properties, *J. Colloid Interface Sci.*, 2022, **633**, 836–850.
52 S. Shen, T. Ke, D. Fang and D. Lin, N and S co-doping of $TiO_2$@C derived from *in situ* oxidation of $Ti_3C_2$ MXene for efficient persulfate activation and sulfamethoxazole degradation under visible light, *Sep. Purif. Technol.*, 2022, **297**, 121460.
53 X. Tian, H. Wu, X. Hu, Z. Wang, C. Ren, Z. Cheng, L. Dou and Y.-W. Lin, Enhanced photocatalytic performance of ZnO/AgCl composites prepared by high-energy mechanical ball milling, *New J. Chem.*, 2022, **46**, 9155–9171.
54 Y. Cheng, L. He, G. Xia, C. Ren and Z. Wang, Nanostructured g-$C_3N_4$/AgI composites assembled by AgI nanoparticles-decorated g-$C_3N_4$ nanosheets for effective and mild photooxidation reaction, *New J. Chem.*, 2019, **43**, 14841–14852.
55 J. Zhang, X. An, N. Lin, W. Wu, L. Wang, Z. Li, R. Wang, Y. Wang, J. Liu and M. Wu, Engineering monomer structure of carbon nitride for the effective and mild photooxidation reaction, *Carbon*, 2016, **100**, 450–455.
56 H. Li, B. Sun, T. Gao, H. Li, Y. Ren and G. Zhou, $Ti_3C_2$ MXene co-catalyst assembled with mesoporous $TiO_2$ for boosting photocatalytic activity of methyl orange degradation and hydrogen production, *Chin. J. Catal.*, 2022, **43**, 461–471.
57 X. Zhang, H. Zhang, J. Yu, Z. Wu and Q. Zhou, Preparation of flower-like $Co_3O_4$ QDs/$Bi_2WO6$ p–n heterojunction photocatalyst and its degradation mechanism of efficient visible-light-driven photocatalytic tetracycline antibiotics, *Appl. Surf. Sci.*, 2022, **585**, 152547.
58 S. Li, L. Shao, Z. Yang, S. Cheng, C. Yang, Y. Liu and X. Xia, Constructing $Ti_3C_2$ MXene/$ZnIn_2S_4$ heterostructure as a Schottky catalyst for photocatalytic environmental remediation, *Green Energy Environ.*, 2022, **7**, 246–256.
59 W. Gan, J. Zhang, H. Niu, L. Bao, H. Hao, Y. Yan, K. Wu and X. Fu, Fabrication of Ag/AgBr/$TiO_2$ composites with enhanced solar-light photocatalytic properties, *Colloids Surf., A*, 2019, **583**, 123968.
60 B. Zhou, H. Hong, H. Zhang, S. Yu and H. Tian, Heterostructured Ag/g-$C_3N_4$/$TiO_2$ with enhanced visible

light photocatalytic performances, *J. Chem. Technol. Biotechnol.*, 2019, **94**, 3806–3814.

61 Y. Ren, D. Guo, Z. Zhao, P. Chen, F. Li, J. Yao, H. Jiang and Y. Liu, Singlet oxygen mediated photocatalytic Antimonite decontamination in water using nanoconfined $TiO_2$, *Chem. Eng. J.*, 2022, **435**, 134832.

62 H. Sun, C. Zou and W. Tang, Designing double Z-scheme heterojunction of g-$C_3N_4$/$Bi_2MoO_6$/$Bi_2WO_6$ for efficient visible-light photocatalysis of organic pollutants, *Colloids Surf., A*, 2022, **654**, 130105.

63 H. Huang, N. Huang, Z. Wang, G. Xia, M. Chen, L. He, Z. Tong and C. Ren, Room-temperature synthesis of carnation-like ZnO@AgI hierarchical nanostructures assembled by AgI nanoparticles-decorated ZnO nanosheets with enhanced visible light photocatalytic activity, *J. Colloid Interface Sci.*, 2017, **502**, 77–88.

64 Y. Wang, H. Yang, H. Yun, J. Gao, Y. Liu, M. Zhang, G. He and Z. Sun, Crystallization time-induced microstructural evolution and photoelectrochemical properties of ternary Ag@AgBr/$TiO_2$ nanorod arrays, *J. Alloys Compd.*, 2022, **904**, 163370.

65 B. Chen, X. Chen, R. Li, W. Fan, F. Wang, B. Mao and W. Shi, Flame Reduced $TiO_2$ Nanorod Arrays with Ag Nanoparticle Decoration for Efficient Solar Water Splitting, *Ind. Eng. Chem. Res.*, 2019, **58**, 4818–4827.

66 K. Dai, D. Li, L. Lu, Q. Liu, C. Liang, J. Lv and G. Zhu, Plasmonic $TiO_2$/AgBr/Ag ternary composite nanosphere with heterojunction structure for advanced visible light photocatalyst, *Appl. Surf. Sci.*, 2014, **314**, 864–871.

67 Y. Wan, C. Liang, Y. Xia, W. Huang and Z. Li, Fabrication of graphene oxide enwrapped Z-scheme $Ag_2SO_3$/AgBr nanoparticles with enhanced visible-light photocatalysis, *Appl. Surf. Sci.*, 2017, **396**, 48–57.

68 V. Q. Hieu, T. K. Phung, T. Q. Nguyen, A. Khan, V. D. Doan, V. A. Tran and V. T. Le, Photocatalytic degradation of methyl orange dye by $Ti_3C_2$-$TiO_2$ heterojunction under solar light, *Chemosphere*, 2021, **276**, 130154.

69 M. A. Hossen, H. M. Solayman, K. H. Leong, L. C. Sim, N. Yaacof, A. Abd Aziz, L. Wu and M. U. Monir, Recent progress in $TiO_2$-Based photocatalysts for conversion of $CO_2$ to hydrocarbon fuels: A systematic review, *Results Eng.*, 2022, **16**, 100795.